Time-dependent density-functional-theory calculations of the nonlocal electron stopping range for inertial confinement fusion applications

K. A. Nichols, S. X. Hu, A. J. White, V. N. Goncharov, D. I. Mihaylov, L. A. Collins, N. R. Shaffer, and V. V. Karasiev

Phys. Rev. E **108**, 035206 — Published 8 September 2023

DOI: 10.1103/PhysRevE.108.035206

Time-dependent density-functional-theory calculations of the nonlocal electron stopping range for inertial confinement fusion applications

K. A. Nichols,[1,2] S. X. Hu,[1,2,3,*] A. J. White,[4] V. N. Goncharov,[1,3] D. I. Mihaylov,[1] L. A. Collins,[4] N. R. Shaffer,[1] and V. V. Karasiev[1]

[1]*Laboratory for Laser Energetics, University of Rochester, Rochester, New York 14623-1299, USA*

[2]*Department of Physics and Astronomy, University of Rochester, Rochester, New York 14623-1299, USA*

[3]*Department of Mechanical Engineering, University of Rochester, Rochester, New York 14623-1299, USA*

[4]*Los Alamos National Laboratory, Los Alamos, New Mexico 87545, USA*

**Corresponding author; Email: shu@lle.rochester.edu*

ABSTRACT

Nonlocal electron transport is important for understanding laser-target coupling for laser-direct-drive (LDD) inertial confinement fusion (ICF) simulations. Current models for the nonlocal electron MFP in radiation-hydrodynamic codes are based on plasma-physics models developed decades ago; improvements are needed to accurately predict the electron conduction in LDD simulations of ICF target implosions. We utilized time-dependent density-functional-theory (TD-

DFT) to calculate the electron stopping power (ESP) in the so-called "conduction zone" plasmas of polystyrene in a wide range of densities and temperatures relevant to LDD. Compared to the modified Lee–More model, the TD-DFT calculations indicated a lower SP and a higher stopping range for nonlocal electrons. We fit these ESP calculations to obtain a global analytical model for the electron stopping range as a function of plasma conditions and the nonlocal electron kinetic energy. This model was implemented in the 1-D radiation-hydrodynamic code, *LILAC*, to perform simulations of LDD ICF implosions, which are further compared to simulations by the standard modified Lee–More model. Results from these integrated simulations are discussed in terms of the implications of this TD-DFT based mean-free-path model to ICF simulations.

I. INTRODUCTION

Inertial confinement fusion (ICF) research has reached significant milestones in the past few years including achieving a burning plasma state [1,2] and obtaining a target gain $G > 1$ [3] using the indirect-drive scheme. The ICF community suggests that laser direct drive (LDD) is a viable method to obtain a high gain with inexpensive targets. In the LDD scheme of ICF, target acceleration relies on the thermal conduction of electrons which absorb laser energy in coronal plasmas and then transfer these energies to the ablation front of the target. The plasma region between the location of critical electron density and the ablation front is called the "conduction zone" in LDD. Nonlocal electrons (E_k = 10 to 20 keV) heated by intense laser light in the coronal plasmas will transverse the conduction zone to provide the ablation pressure for ICF target implosions. Understanding how these nonlocal electrons lose energy in the conduction-zone plasma is crucial for understanding laser–target coupling in LDD ICF modeling [4]. In LDD, a typical ICF target consists of deuterium-tritium (DT) gas, enclosed by a solid mixture of

DT, and encapsulated by a thin ablative shell of polystyrene (CH). As intense laser beams illuminate the ICF target, the CH layer is heated and ablated; shocks are launched to compress the DT layer; the continuous laser ablation accelerates the target to implode up to a high velocity of $v_{imp} > 3.7 \times 10^7$ cm/s [5].

During this laser-ablation process, the laser energy is absorbed in the coronal plasma below the critical surface and carried to the ablation front in the form of high-energy electrons; the critical surface is the radius that coincides with the critical electron density (in CH, this corresponds to a mass density, $\rho_c \approx 0.04 \text{g/cm}^3$) [6]. As these energetic and nonlocal electrons move through the conduction zone, they interact with and lose energy to the background CH and DT plasmas. In some cases, the electrons reach thermal equilibrium with the CH or DT. In this paper, we define the stopping range or mean free path (MFP) of a nonlocal (projectile) electron as the distance it travels before its velocity drops to the electron thermal velocity of the background plasma. Thus, understanding and calculating the nonlocal electron MFP is crucial for accurate simulations of ICF experiments and understanding laser–target energy coupling.

Over the past few decades, different models based on traditional plasma physics have been developed to model the nonlocal thermal transport for high-energy-density (HED) plasmas [7-10]. For instance, the current model for nonlocal electron thermal conduction in the 1-D radiation-hydrodynamic code *LILAC* [11], is a modified version of the Lee–More method [10,12]. As shown in Ref. [12], the conduction model inaccurately predicts the optical depth modulation, among other quantities, compared to experimental results performed on OMEGA. More recently, experimental evidence has also indicated that the CH–DT interface retreats differently between experiments and *LILAC* simulations [13,14]. These observations have

motivated us to seek a more-accurate model of the nonlocal electron MFP to improve the predicative capability of LDD implosion simulations.

Stopping power, SP = (–dE/dx), is directly related to the nonlocal electron stopping range; the nonlocal electron is treated as the projectile stopping in a given material [12]. There are many analytical formulas that model the SP of ions in classical and quantum materials including the Li–Petrasso method [15], the Brown–Preston–Singleton method [16,17], and the dielectric function formalism [18]. These models, although computationally inexpensive, are established by the homogeneous electron gas and generally neglect any partial ionization effects. They also fail to incorporate phenomena including the Barkas effect [19,20] and Z_1 oscillation [21]. The former accounts for the fact that SP is dependent on the sign of the projectile's charge; meaning under the same conditions, a proton and an antiproton would exhibit distinct SPs [19,20]. The latter accounts for the oscillations of the SP due to the projectile's charge [21]. Thus, we turn to *ab initio* methods such as the time-dependent density-functional-theory (TD-DFT), including the orbital-free (OF) and stochastic Kohn–Sham schemes, to calculate the nonlocal electron SP and MFP.

In this paper, we will outline the TD-OF-DFT algorithm [22], in Sec. II, accompanied by a brief discussion of the time-dependent stochastic DFT. In Sec. III, we present the SP and MFP results from direct TD-DFT calculations of nonlocal electron stopping in conduction-zone CH plasmas relevant to LDD ICF. We then fit these TD-DFT results to obtain our global, analytical model with numerical coefficients for the nonlocal electron MFP. These results are compared to other SP models as well as the modified Lee–More model currently used in *LILAC* [12]. In Sec. IV, we implement this global and TD-DFT based MFP model into *LILAC* and demonstrate its effect on LDD implosions through *LILAC* simulations. The simulation results are also discussed.

Finally, we summarize these findings in Sec. V, and include additional discussions and plans for improvement.

II. METHODOLOGY

A. Time-dependent density functional theory

The first principle TD-DFT has been applied to perform calculations for different dynamic properties of plasmas [23-26]. Thus, TD-DFT has been used to reproduce and obtain SP results in warm dense matter [27-31]. Our SP calculations are performed using the OF approach to TD-DFT [32]. While the Mermin-Kohn-Sham (MKS) approach to DFT [33,34] is more accurate than the OF method; the MKS method has computational costs that scale cubically with volume and temperature [28,33]. Moreover, the temperature regime we consider for an ICF polystyrene plasma (100 to 1000 eV) is extreme enough that the orbital-free treatment becomes reasonably accurate [22]. Thus, for the sake of computational resources and time, we mostly utilized TD-OF-DFT for our simulations. We benchmarked some of our calculations using time-dependent stochastic density-functional-theory (TD-sDFT). Overall, our TD-DFT results of nonlocal electron SP (and stopping range) are obtained using the recently developed stochastic and hybrid representation electronic structure by density functional theory (*SHRED*) code [19].

The OF method for DFT follows a similar approach to the Kohn–Sham approach to DFT. However, in the OF-DFT method, the electron density, $\rho(\mathbf{r})$, is represented using a single, collective orbital $|\psi(\mathbf{r})|^2 = \rho(\mathbf{r})$, while in the Mermin–KS approach, the density is defined as a sum of many noninteracting orbitals $\rho(\boldsymbol{r}) = \sum_n f_n \psi_n^*(\boldsymbol{r})\psi_n(\boldsymbol{r})$ for Fermi–Dirac occupations, f_n. We can extend this OF approach to include time-dependent effects by defining the orbital using

the scalar velocity field $\nabla S(\boldsymbol{r},t)$ such that $\psi(r,t) = \sqrt{\rho(\boldsymbol{r})} \cdot e^{iS(\boldsymbol{r},t)}$; we write the time-dependent version of the single particle Schrodinger-like equation as [22,30]:

$$i\frac{\partial \psi(\mathbf{r},t)}{\partial t} = \left[\frac{-\nabla^2}{2} + \hat{V}_{\text{eff}}(\mathbf{r},t)\right]\psi(\mathbf{r},t). \tag{1}$$

In the above equation, the effective potential [for $\rho = \rho(\boldsymbol{r},t)$] is defined as

$$\hat{V}_{\text{eff}}(\boldsymbol{r},t) = V_H(\rho,\boldsymbol{r}) + \frac{\delta F_{\text{s-vW}}^{TF}[\rho]}{\delta\rho} + \frac{\delta E_{\text{xc}}[\rho]}{\delta\rho} + V_{\text{ext}} \tag{2}$$

and is the sum of the contributions from the mean field Hartree potential, $V_{\text{H}}(\rho,\mathbf{r})$, the Thomas–Fermi plus von-Weizsacker non-interacting free-energy, $\frac{\delta F_{S-vW}^{TF}[\rho,T]}{\delta\rho}$ [35,36], the exchange correlation potential, $\frac{\delta E_{\text{xc}}[\rho]}{\delta\rho}$, and the external potential, V_{ext}, for electron–ion interactions. Equations (1) and (2) give the typical TD-OF-DFT algorithm, which is called Thomas–Fermi–von-Weizsacker approach to TD-DFT. To better catch the time-dependent response, however, we include the addition of current dependent energy density potential $V_{\text{CD}}(\boldsymbol{r},t)$ based on the Lindhard response and defined in [22], to the overall effective potential, $\hat{V}_{\text{eff}}$. As discussed in Ref. [22], the addition of this term is shown to improve the SP calculations near the Bragg peak; moreover, including this dynamic term creates a nonadiabatic version of TD-OF-DFT [22,30].

In addition to the TD-OF-DFT method used for most MFP calculations for nonlocal electrons in conduction-zone CH plasmas, we have also applied TD-sDFT to benchmark some of our TD-OF-DFT calculations. The details about the TD-sDFT method have been given in a recent paper, see Ref, [28,37], here we briefly outline the basics. TD-sDFT calculations [28,38-40], are an extension of the typical MKS method; this method enables high-temperature calculations viable for $T \gg T_{\text{F}}$ (with T_{F} being the Fermi temperature for a given electron density). TD-sDFT, as

described extensively in [28,38,39], uses the Hutchison method to estimate the initial electron density using stochastic Rademacher vectors [40]. When converged, TD-sDFT reaches the same accuracy as the typical KS approach, but as it scales linearly with size and inversely with temperature, it costs much less computationally for the high energy density (HED) systems described in this article.

B. TD-DFT calculations for nonlocal ESP

We use the above TD-DFT algorithm to set up our SP simulations in polystyrene. Equations (1) and (2) are self-consistently solved for both the incoming electron and the background CH plasma using the split operator method [41]. For our simulations we take a single, high-energy electron with different kinetic energies up to 25 keV, and project it along the z-axis into a box of CH plasmas with a given temperature and mass density. To account for relativistic effects, we use the Einstein relation for kinetic energy, $K = ((pc)^2 + (mc^2)^2)^{1/2} - mc^2$, to determine the corresponding input velocity from the momentum, $p = \gamma v m$ with γ being the Lorentz factor.

For each density–temperature condition, we perform convergence tests for the time step, grid size, and box size. For the sake of computational and time resources, we have converged our TD-DFT calculations to ~10% accuracy. Our simulations are run for boxes between 256 to 320 atoms and a ratio of [1:1:(4 to 5)] for the simulation box lengths of L_x, L_y, and L_z. Thus, the length of the box along the direction of motion (z) ranges from 44.22 Å to 96.03 Å. The time step for TD-DFT calculations is 3×10^{-3} atomic units $\cong 7.26 \times 10^{-5}$ fs. Moreover, the grid points in the x-direction are between 128 and 320. The grid spacing is directly related to the energy cutoff, [28] which defines the max energy of the plane-wave basis.

We have used the Perdew–Burke–Ernzerhof (PBE) exchange-correlation functionals [42] implemented through the LibXC package [43]. For our calculations, pseudopotentials are used; for carbon we use an all-electron Hartwigsen-Goedeker-Hutter (HGH) pseudopotential and for hydrogen we utilize the Goedecker pseudopotential [44-47]. Furthermore, for the electron projectile we utilize the same pseudopotential as the hydrogen (proton); however, we take the charge to be "–1" and, in our simulation, set the mass to be the electron mass. Thus, the incoming electron is treated as a classical particle with a negative charge and mass of an electron, while the background electrons are treated quantum mechanically. The approximation that the electron projectile is treated classically in our current TD-DFT calculations, should be reasonable as nonlocal thermal transport is mainly concerned with energetic electrons (~6kT), significantly more energetic than the background plasma electrons (~kT).

We have used orbital-free density-functional theory molecular-dynamics (OFMD) simulation to generate different configurations of the background CH plasma. Namely, for a given mass density, plasma temperature, and box size, the C and H atoms are randomly positioned into the simulation box; finite-temperature DFT calculations determine the mean-field electron density for a given ionic configuration, from which the Hellman-Feynman theorem will tell you the electronic force acting on each ion. Combining the electronic force with the ionic forces, the total force will move each ion to its new location for a given time step by classical Newton's equation. Such a MD process is repeated thousands of time steps to sample different configurations of the background CH plasma. This *ab initio* DFT-MD method [48-50] has extensively been used to simulate plasmas ranging from warm-dense matter to ideal plasmas in the past two decades. For the results presented here, the CH plasma density varies from 0.05-g/cm^3 to 1.0-g/ cm^3 and temperature ranges from 100-eV to 1000 eV, corresponding to plasma

types varying from partially ionized non-ideal ones to ideal plasmas. As shown in Fig. 1, since OFMD simulations go beyond the homogeneous electron gas, we see slight fluctuations in the electron density. With the OFMD-generated configurations, we take evenly spaced time snapshots of the background plasma for TD-DFT calculations through which the nonlocal electrons propagate. For each TD-DFT simulation, the positions of the ions are held constant because the time of projectile passing through the plasma is short (~fs). The stopping power is then computed using TD-DFT as the average TD mean field force on the electron projectile at a given time using the Hellman-Feynman theorem [22,28] such that : $\frac{dE}{ds} = < F_{proj}(\rho, \boldsymbol{R}, t) >$, where the vector $\boldsymbol{R}$ is the position of the projectile computed using classical equations of motion. The full force equation given in [22,28].

Moreover, the average force on the projectile is directly related to the SP defined as:

$$-\frac{dE}{dz} = -\frac{dE}{ds} cos(\theta_D) \tag{3}$$

where θ_D is the electron's angle of deflection (discussed below) and dE/ds is defined above. There are two ways to compute the stopping power in TD-DFT calculations: one where the projectile is propagated through the plasma at a constant velocity and the other where the projectile can change velocity as it propagates causing deflection/scattering to occur. For heavy ion projectiles, both methods will give similar results as the deflection effect is negligible. However, for a light electron projectile we must incorporate this deflection angle. To obtain dE/ds, we run the above simulation with the projectile's momentum fixed solely in the z-direction. We then run a second simulation to allow the electron to scatter to obtain the deflection angle, θ_D, discussed below. Combining these two results we obtain our SP given in equation (1). To improve our statistics, we allow the electron projectile to pass through the z direction of the box multiple times (10 passes); starting at the time it takes for the electron to

reach $L_z/8$, we continuously calculate the rolling average force, $< \frac{dE}{ds} >$, on the electron. After the simulation has ended, we take the mean of the rolling average measurements as the value, $\frac{dE}{ds}$, for the given conditions; we exclude the rolling average measurements from the first 2 passes (up to $2L_z$) in our second average to avoid extremes caused by the initial oscillatory behavior of the SP. For most results presented here, we have averaged over at least two snapshots of the background CH plasma. Because the conduction zone plasmas are approaching a weakly coupled case, we find that different snapshots yield very similar SP results.

To give an example of these TD-DFT calculations, Fig. 1 shows time snapshots of the difference between the instantaneous and initial electron density in the *y*–*z* plane for a single electron stopping in CH at 0.50 g/cm^3, 500 eV. In this figure, we allow the electron to change velocity as it moves through the plasma. The white dotted line shows the undeflected path of the electron; each box contains 320 atoms with a 1:1:5 ratio between L_x, L_y, and L_z. Figs. 1(a)–1(c) show time snapshots for an electron projectile with 6 keV initial kinetic energy; Figs. 1(d)–1(f) are time snapshots for an electron with an initial kinetic energy of 20 keV. For every run, the electron projectile starts from the location $\left(L_x/2, L_y/2, 0\right)$. We see the trajectory of the nonlocal electron as it propagates along the z axis and interacts with the background CH plasma. The projectile electron leaves a clear wake as it progresses through the CH plasma. This kind of plasmonic behavior, as discussed in [51], induces a "drag" force on the projectile due to dynamic response that contributes to the overall stopping power and is included in our TD-DFT calculations. Furthermore, as the incoming electron moves along the z direction of the box, it is scattered in the x and y directions. This deflection is apparent for low-velocity projections [see Figs. 1(a)–1(c)], but when the electron projectile velocity is much larger than the thermal

velocity of the background electrons ($v_{\text{proj}} \gg v_{\text{th}}$), the deflection is less significant to the overall stopping [see Figs. 1 (d)–1(f)]. For all incoming electrons, we calculate this angle of deflection, θ_D, such that: $cos(\theta_D) = \frac{\Delta z}{\sqrt{\Delta x^2+\Delta y^2+\Delta z^2}}$, where Δx, Δy, and Δz are the distances the electron projectile has moved from its initial point. To calculate this deflection angle for a given set of plasma conditions, we run the same simulation as discussed above, however we allow the electron to accelerate/decelerate as it travels through the polystyrene. We look at the trajectory of the electron, to calculate the angle of deflection. Similar to our calculations of dE/ds, we take the rolling average of cos(θ_D); however, we only calculate θ_D until either the electron is deflected past the length of L_x or L_y, or until one complete pass in the z direction. Again, we take the mean of the rolling average values as the final value of θ_D. Different from the dE/ds measurements, we generate θ_D using only one ionic configuration for each set of distinct (ρ, T, K). Finally using our obtained values for θ_D and $\mathrm{dE/ds}$, we calculate the SP defined in Equation (3).

C. The modified Lee–More model for the mean free path of nonlocal electrons

To investigate the implications of our TD-DFT results to LDD implosion simulations, we discuss the current nonlocal electron conduction model used in radiation-hydrodynamic codes for ICF target design and simulations in this subsection. A modified version of the Lee–More model [10,12] has been used to calculate the nonlocal electron transport in the 1-D hydrocode LILAC; the general algorithm for this previously established method is discussed below. Moreover, we note that by fully examining the formulation, the velocity scaling of the collective Coulomb logarithm can properly approach the classical Bohr ($\sim v^3$) or the quantum Bethe ($\sim v^2$) limit [52,53]. With this model, the general electron penetration depth is given as [12]:

$$\lambda_E = \sqrt{\lambda_{\mathrm{K}} \lambda_{90}}, \tag{4}$$

where

$$\lambda_k \frac{K^2}{4\pi e^4 \left(n_{\mathrm{e}}^T \Lambda_{\mathrm{e}} + n_{\mathrm{e}}^{\mathrm{f}} \Lambda_{\mathrm{c}} \right)}, \tag{5}$$

$$\lambda_{90} = \frac{K^2}{2\pi e^4 \left(\Lambda_{\mathrm{e}} + Z\Lambda_{\mathrm{i}}/2 \right)} \tag{6}$$

are the electron deposition path and 90° scattering path defined as a function of the non-local (projectile) electron kinetic energy, K, the total and free-electron densities $\left(n_{\mathrm{e}}^T, n_{\mathrm{e}}^{\mathrm{f}} \right)$, and the specified Coulomb logarithm (CL). The electron–ion and electron–electron CLs are defined as,

$$\Lambda = \log\left(\frac{b_{\max}}{b_{\min}} \right) \tag{7}$$

using the maximum $b_{\max}$ and minimum $b_{\min}$ impact parameters for Coulomb scattering such that

$$b_{\max} = \max\left[\lambda_{\mathrm{D}}, \left(3/4\pi n_{\mathrm{i}} \right)^{1/3} \right], \tag{8}$$

$$b_{\min}^{\mathrm{i}} = \max\left(\frac{\hbar}{m_{\mathrm{e}} v}, \frac{\langle Z \rangle e^2}{2K} \right), \; b_{\min}^{\mathrm{e}} = \max\left(\frac{\hbar}{m_{\mathrm{e}} c} \sqrt{\frac{2}{\gamma - 1}}, \frac{e^2}{2K} \right). \tag{9}$$

Above, λ_D is the Debye length, n_i is the ion density, and γ is the Lorentz factor. Each of the above parameters reflects a physical limit; b_{max} is determined by either the Debye length or the average ion radius to account for screening. The parameter b_{min} is defined as a function of the particle energy; at low energy it is the minimum impact parameter by a classical electron, while at high energy it is the minimum distance constrained by the uncertainty principle [10,12]. Furthermore, the CL due to collective effects is defined as

$$\Lambda_c = \log\left(1.123v/\omega_p b_{max}\right), \tag{10}$$

for plasma frequency ω_p and projectile velocity v. For highly ionized plasmas this effectively replaces b_{max} with a velocity-dependent cutoff.

The original Lee–More method is based upon the kinetic Boltzmann equations and neglects electron–electron scattering, thus the algorithm becomes inaccurate for low-Z materials; however, the modified version, although still based on the Boltzmann equations, has been updated to include electron–electron collisions as shown in Eqs. (4)–(6) [10]. This method, while computationally simple, does not accurately predict the MFP of nonlocal electrons, as evidenced by experimental soft x-ray self-emission images in cryogenic DT implosions on OMEGA [14]. Our *ab initio* TD-DFT calculations are intended to examine if there is any deviation from the modified Lee–More model for nonlocal electrons traversing the conduction-zone CH plasmas in LDD implosions.

III. RESULTS

A. Electron stopping power in "conduction-zone" polystyrene plasmas

Using the above TD-OF-DFT methodology, we obtain SP results for a high-energy electron traversing the CH plasma for ICF conditions. Prior to developing our global model for the MFP, we looked directly at our SP data obtained from TD-OF-DFT calculations. We probed seven unique density–temperature conditions on CH plasmas at mass densities of 0.05 g/cm^3 to 1.0 g/cm^3 and temperatures of 100 eV to 1000 eV, with nonlocal electron ("projectile") kinetic energy values up to 25 keV. These unique plasma conditions span the necessary "conduction-zone" regime. Since TD-DFT calculations are computationally expensive, we computed (–dE/ds) for 10 to 12 distinct nonlocal electron kinetic energy values for each unique plasma condition. Fig. 2 shows the SP (–dE/dz) distributions for each of these plasma conditions. The individual points represent the exact TD-OF-DFT calculations with the deflection angle considered; the corresponding curves are the individualized fits. Each of the points in Fig. 2 corresponds to the stopping power averaged over two snapshots, meaning that for each projectile kinetic energy value we have repeated the TD-OF-DFT calculations with two different configurations of the background CH plasma. The two-snapshot calculations generally resulted in distinct, but similar SP results. Here, we interpolate/fit each set of data using the sum of multiple, (i), weighted Gaussian distributions: $\mathrm{SP} = \sum_i a_i \mathrm{e}^{-(K-b_i)^2/2c_i^2}$ with numerically determined coefficients (a_i,b_i,c_i) to interpolate the data. Such fitting serves solely as an interpolation of each TD-DFT data set, which enables the numerical integration for calculating the mean free path of nonlocal electrons. The small inaccuracy near the high-energy endpoint would not significantly affect the mean-free path calculations, shown by the integration in Eq. (11).

Moreover, in Fig. 3 we compare our TD-DFT results for a CH plasma at 0.50 g/cm^3, 500 eV to the Brown–Preston–Singleton (BPS) [16,17], Li–Petrasso (LP) [15], and dielectric function (DF) [18] methods for SP. We note that while the three analytical models assume a uniform

electron density, the TD-DFT results, as shown in Fig. 3, allow for fluctuations in the electron density along the trajectory of the electron. Overall, we see that for the highly energetic electrons, TD-DFT predicts considerably smaller stopping power compared to all three analytical models by a factor of ~2. We note that previous results of ion stopping in warm dense matter, showed that TD-DFT exhibited lower stopping power by ~15%-25% compared to traditional plasma models [22,27,30]. Furthermore, previous experimental results on proton stopping, [29, 30, 31] showed that TD-DFT calculations (in both the KS and OF formulation) not only aligned well with experimental data but outperformed analytical models including BPS, LP, and DF.

To understand what causes this lower SP, we have explored the background electron density along the projectile's trajectory in TD-OF-DFT simulations. The resulting distribution, however, averaged out to the uniform electron density assumed by the usual plasma models. The Barkas effect can partially explain the large discrepancy between TD-DFT calculations and analytical models. The Barkas effect considers that a negatively charged projectile has a lower SP compared to a positively charged projectile of the same mass. Traditional plasma models for SP typically assume the projectile is positively charged, or that the sign of the projectile's charge does not matter if the first-Born approximation is invoked; however, TD-DFT goes beyond this assumption [19,20,54]. To quantify this effect, we performed TD-OF-DFT calculations for a high energy positron moving in a CH plasma of 0.50 g/cm^3 and 500 eV temperature. We tested the positron projectile energies of 2keV, 6keV, and 12keV. The results showed, compared to the electron projectile case, the positron exhibited a ~17-42% relative increase in stopping power. Thus, this Barkas effect can partially explain the lower SP using TD-DFT calculations compared to the traditional plasma models.

Finally, in Fig. 3 we benchmark our SP results to TD-sDFT [28,38-40], briefly described above and fully derived in Ref [28]. For our TD-sDFT calculations, shown in orange, we use 200 stochastic orbitals and keep all remaining parameters (time step, box size, ion configuration, etc.) the same as our TD-OF-DFT calculations. For the sake of computational resources, we only validate a few points. Again, we take the rolling average SP with respect to time starting at the time for the electron to progress to $L_z/8$. We take the average of the rolling average SP, beginning at the time it takes the electron to progress to $3L_Z$; then remove the first three passes to minimize the contribution of the initial stochastic fluctuations to the overall stopping. For the stochastic points, we allow the electron to accelerate/decelerate while it progresses through the plasma and take the SP shown in Eq. (3), where θ_{D} is the same angle determined by the TD-DFT calculations. Fig. 3 indicates that the stochastic results align well with the TD-OF-DFT results, indicating that the TD-OF-DFT algorithm is in fact valid in this extreme temperature regime (degeneracy parameter: $\theta \gg 1$, $T \geq 100$ eV).

B. Nonlocal electron mean free path

We utilize our generalized SP data to derive a global model for the nonlocal electron deposition path (range) based on our plasma parameters and initial nonlocal electron kinetic energy. The SP calculations are directly related to the MFP, λ_E using the integral

$$\lambda_E = \int_{\frac{3}{2}k_bT}^{E_0} \frac{\mathrm{d}E}{-\mathrm{d}E/\mathrm{d}z}, \tag{11}$$

where E_0 is the initial kinetic energy of the electron, T is the temperature of the background plasma, and $-dE/dz$ is our SP. We denote the MFP as the distance before the nonlocal electron loses enough energy to the plasma that it reaches thermal equilibrium [$E_0 < (3/2)k_bT$] with the background electrons. Thus, the low-energy limit for integration in Eq. (11) is taken to be $(3/2)k_bT$ rather than zero. Moreover, we take the MFP to be zero for any nonlocal electrons with [$E_0 < (3/2)k_bT$]. Using this integral, and our interpolated SP data, we obtain mean-free-path data for all the CH plasma densities and temperatures examined. Then, we fit the overall mean-free-path data set to a single, analytical model with numerically determined coefficients.

Our model is dependent on the plasma temperature, T, density, ρ, and initial nonlocal electron kinetic energy, K. We normalize the plasma parameters, (T, ρ) with values within the "conduction zone," and use numerically determined coefficients [55]; the coefficients a_0, b_0, c_0, e_0, f_0, α, β, γ, δ, ε, ζ, ω, $\phi_{1,2}$ and $\psi_{1,2}$ are given in Table I to four significant figures. In general, the TD-OF-DFT based model takes the form:

$$\lambda_E = K^2 \left\{ \frac{\langle Z \rangle^2 a_0}{4\pi e^4 n_e} \left(\frac{K}{\langle Z \rangle} \right)^a \left[b_0 \left(\frac{T}{400} \right)^\beta \left(\frac{\rho}{0.450} \right)^\gamma \right. \right. \\ \left. \left. + c_0 K^\delta \left(\frac{T}{400} \right)^\varepsilon \left(\frac{\rho}{0.450} \right)^\zeta \right] + d_0 \log(K+1)^\omega \right\} \tag{12}$$

for, $\lambda_E = \lambda_E(\rho, T, K)$. The temperature is given in units of eV and the incoming electron kinetic energy K is given in keV. The mass density, ρ, electron density, n_e, elementary charge, e, and any remaining physical constants are in CGS units. Moreover, the coefficient d_0 is dependent on the average ionization state $\langle Z \rangle$ of the background plasma

$$d_0 = \begin{cases} f_0 \left(\dfrac{T}{400} \right)^{\phi_1} \left(\dfrac{\rho}{0.450} \right)^{\psi_1} & \dfrac{Z_{\max} - \langle Z \rangle}{Z_{\max}} < 0.05 \\ e_0 \left(\dfrac{T}{400} \right)^{\phi_2} \left(\dfrac{\rho}{0.450} \right)^{\psi_2} & \text{else} \end{cases} \tag{13}$$

such that d_0 is evaluated one way if $\langle Z \rangle$ falls within 5% of the completely ionized state, $Z_{\max}$ = 3.5, and another otherwise. We keep the same initial pre-factor as the modified Lee–More method, shown in Eqs. (4)–(6); the average ionization, $\langle Z \rangle = \langle Z(\rho, T) \rangle$, is defined using the first-principles approach introduced in Ref. [56].

Fig. 4 shows the global model (solid curves) and the corresponding TD-DFT data (individual points) for each of the seven density/temperature conditions probed. We see the model reaches overall agreement for the higher nonlocal electron energies (5 to 20 keV), which are closely relevant to the nonlocal transport in LDD conduction-zone conditions. Using this model obtained from our TD-DFT data, we can predict the nonlocal electron MFP for a wide range of plasma conditions relevant to ICF polystyrene plasmas in LDD implosions.

IV. MODEL COMPARISON

To see the effects of our TD-DFT-based nonlocal electron mean-free-path model on ICF simulations, we compare our results directly to the modified Lee–More method and implement it into a 1-D radiation-hydrodynamic code *LILAC*. The modified Lee–More method, defined by Eqs. (4)–(10), has been used for the past decades in *LILAC*, to predict nonlocal thermal transport. As an illustrative example, our nonlinear model fits of TD-OF-DFT results [Eq. (12)] of λ_E are compared with the Lee–More results [Eq. (4)] [12] in Fig. 5 as a function of the

nonlocal electron kinetic energy. Fig. 5 shows the TD-OF-DFT data (points), the corresponding nonlinear model fit, and the modified Lee–More method for a single electron stopped in CH plasma at 0.10 g/cm^3 and at temperatures of (a) 300 eV or (b) 1000 eV. Evidently, we see a large difference when we compare our model to the modified Lee–More method; similar to what we saw in Fig. 3, we note that this difference is a factor of ~2. This indicates that highly energetic electrons (>5 keV) will penetrate the same CH plasma further than currently predicted, thus carrying more laser energy deeper into the conduction-zone plasma. For low-energy electrons, <5 keV), their mean free paths are smaller than what the modified Lee–More predicts. This will evidently change the prediction of laser–target coupling since it is heavily dependent on thermal conduction [14,57] as discussed below.

With the fitted model of TD-OF-DFT results being implemented into *LILAC*, we can further examine how this new model affects simulations of LDD implosions. Specifically, by comparing LDD target simulations using either our TD-DFT based model for the nonlocal electron MFP or the traditional modified Lee–More model for nonlocal electron transport, we can identify its effects on the laser–target coupling and the overall implosion dynamics. For our simulations shown in Fig. 6, the target consists of an 8.0-μm thick CH shell with an initial density ρ_0 = 1.05 g/cm^3 and outer radius, r =438 μm. The layer of DT ice is 50-μm thick with an initial mass density of ρ_0 = 0.254 g/cm^3, while the capsule is filled with DT gas. The target is shown in Fig. 6 and the inset gives the schematic of the OMEGA scale target. The total laser energy is ~26 kJ, which drives the shell to implode with a maximum velocity of v_{imp}~400 km/s. In our simulations, we utilize the nonlocal thermal transport model, iSNB [9], for which the electron MFP takes either our TD-OF-DFT-based model or the original modified Lee–More model based upon the material. Moreover, the crossbeam energy transfer (CBET) model [40] for

laser energy absorption is invoked. We utilize the first-principles equation-of-state and opacity tables given in Refs. [58-61] to describe the CH and DT target materials.

To understand the effects of MFP models (the TD-OF-DFT–based model developed in this work versus the modified Lee–More model), we directly compare the density profile and ablation pressure at 2.1 ns from the two *LILAC* simulations in Fig. 7. In Fig. 8 we show the comparison of overall implosion performance. In both Figs. 7 and 8, the red curves represent the *LILAC* simulation using the TD-OF-DFT–based model, while the blue curves are the *LILAC* simulations using the standard modified Lee–More model to describe the nonlocal electron thermal conduction. In Fig. 7 we observe that the TD-OF-DFT model gives an ~12% relative increase in ablation pressure from the standard *LILAC* simulation, implying the shell has been accelerated further inward. This is consistent with the fact that TD-OF-DFT model predicts a larger MFP for nonlocal electrons, leading to higher nonlocal thermal conduction. The density profile of the shell is very similar for both simulations; however, the density shell in the standard LILAC simulation peaks at a larger shell radius compared to the one using the modified Lee–More model.

Fig. 8(a) shows both the shell velocity (left axis, solid curves) and the compression ρR (right axis, dashed curves) as a function of time for the two *LILAC* simulations. We note a clear time shift to earlier bang for our model when compared to the traditional Lee-More model. This is because the TD-DFT predicted mean-free path of nonlocal electrons is larger than the Lee-More model for projectile electron energies above 3-keV, as indicated by Fig. 5. Thus, these nonlocal electrons in the TD-DFT model travel further in the conduction-zone CH plasmas and closer to the ablation front, thereby delivering more energy to drive the target with a higher ablation pressure (Fig. 7). Furthermore, as we predict an increase in laser energy penetrating the

shell, the target is compressed to its peak areal density earlier compared to the traditional model, thus causing this leftward shift. Consequently, the imploding shell accelerates faster in TD-DFT based simulations than the Lee-More case, resulting in a higher implosion velocity [Fig. 8(a)]. That explains the earlier stagnation and bang time in the TD-DFT based simulation shown in Fig. 8. Using our TD-OF-DFT model for the nonlocal stopping range, we observe a nearly 40% relative increase in the neutron yield from the traditional Lee-More model. In general, we observe significant differences in ICF implosion dynamics when we compare 1-D *LILAC* simulations using our TD-DFT based model with the current modified Lee–More method for electron stopping range. Radiation-hydrodynamic simulations of ICF implosions are highly integrated, meaning they involve many interconnected physics models. This updated nonlocal thermal conduction model will provide a basis for further calibrating other physics models in the code, such as laser absorption, CBET, equation-of-state (EOS), and radiation transport. Aligning these improvements with experiments will be the ultimate goal to improve the predictive capabilities of radiation-hydrodynamic codes for reliable ICF target design and simulations.

V. CONCLUSIONS

In this work, we devised a global analytical model for the nonlocal electron stopping range in polystyrene plasmas for ICF applications based on time-dependent TD-OF-DFT calculations. Specifically, our model is applicable for conduction-zone CH plasmas ranging from 0.05 g/cm^3 to 1.0 g/cm^3 and 100 eV to 1000 eV. Our TD-OF-DFT results showed lower SP and increased stopping range when compared to analytical models. We implemented this model into the 1-D radiation-hydrodynamic code *LILAC* and performed 1-D simulations using a typical OMEGA cryogenic DT target to illustrate its effect on ICF implosions. The results show that the

TD-OF-DFT model yielded large differences in terms of implosion dynamics and target performance when compared to the currently implemented nonlocal transport model of the modified Lee–More stopping range. The new TD-OF-DFT model gives ~12% higher ablation pressure due to longer stopping range of nonlocal electrons, which leads to ~18% faster implosion and ~40% neutron yield than those of the standard *LILAC* simulation. Reconciling these results with experimental observables, such as trajectory measurements and overall target performance, will require further "recalibration" of other physics models used in radiation-hydrodynamics codes, such as the CBET model for laser absorption, EOS, and radiation transport. We hope this work provides the nonlocal thermal transport basis for these recalibration tasks in future studies.

VI. AKNOWLEDGMENTS

This material is based upon work supported by the Department of Energy National Nuclear Security Administration under Award No. DE-NA0003856, the University of Rochester, and the New York State Energy Research and Development Authority. This report was prepared as an account of work sponsored by an agency of the U.S. Government. Neither the U.S. Government nor any agency thereof, nor any of their employees, makes any warranty, express or implied, or assumes any legal liability or responsibility for the accuracy, completeness, or usefulness of any information, apparatus, product, or process disclosed, or represents that its use would not infringe privately owned rights. Reference herein to any specific commercial product, process, or service by trade name, trademark, manufacturer, or otherwise does not necessarily constitute or imply its endorsement, recommendation, or favoring by the U.S. Government or any agency

thereof. The views and opinions of authors expressed herein do not necessarily state or reflect those of the U.S. Government or any agency thereof.

This work is supported by the U.S. Department of Energy through the Los Alamos national Laboratory, operated by TRIAD National Security LLC for the National Nuclear Security Administration (Contract No. 89233218CNA000001).

REFERENCES

[1] H. Abu-Shawareb *et al.*, Physical Review Letters **129**, 075001 (2022).
[2] A. B. Zylstra *et al.*, Nature **601**, 542 (2022).
[3] in *DOE National Laboratory Makes History by Achieving Fusion Ignition* (Department of Energy, 2023).
[4] E. M. Campbell *et al.*, Philos Trans A Math Phys Eng Sci. **379**, 2189 (2021).
[5] R. S. Craxton *et al.*, Phys. Plasmas **22**, 110501 (2015).
[6] S. X. Hu *et al.*, Phys. Plasmas **25**, 082710 (2018).
[7] E. M. Epperlein and R. W. Short, Physics of Fluids B: Plasma Physics **3**, 3092 (1991).
[8] G. P. Schurtz, P. D. Nicolaï, and M. Busquet, Physics of Plasmas **7**, 4238 (2000).
[9] D. Cao, G. Moses, and J. Delettrez, Phys. Plasmas **22**, 082308 (2015).
[10] Y. T. Lee and R. M. More, The Physics of Fluids **27**, 1273 (1984).
[11] J. Delettrez, R. Epstein, M. C. Richardson, P. A. Jaanimagi, and B. L. Henke, Phys. Rev. A **36**, 3926 (1987).
[12] V. N. Goncharov *et al.*, Physics of Plasmas **13**, 012702 (2006).
[13] R. Shah.
[14] R. C. Shah *et al.*, Physical Review E **103**, 023201 (2021).
[15] A. B. Zylstra, H. G. Rinderknecht, J. A. Frenje, C. K. Li, and R. D. Petrasso, Phys. Plasmas **26**, 122703 (2019).
[16] L. S. Brown, D. L. Preston, and R. L. Singleton, Jr, Physics Reports **410** 237 (2005).
[17] R. L. Singleton, Jr, Phys. Plasmas **15**, 056302 (2008).
[18] C. F. Clauser and N. R. Arista, Physical Review E **97**, 023202 (2018).
[19] N. R. Shaffer and S. D. Baalrud, Phys. Plasmas **26**, 032110 (2019).
[20] W. H. Barkas, J. N. Dyer, and H. H. Heckman, Phys. Rev. Lett. **11**, 26 (1963).
[21] M. Pefialba, A. Arnau, and P. M. Echenique, Nuclear Instruments and Methods in Physics Research **67**, 1 (1992).
[22] A. J. White, O. Certik, Y. H. Ding, S. X. Hu, and L. A. Collins, Physical Review B **98**, 144302 (2018).
[23] A. D. Baczewski, L. Shulenburger, M. P. Desjarlais, S. B. Hansen, and R. J. Magyar, Physical Review Letters **116**, 115004 (2016).
[24] K. Jiang and M. Pavanello, Physical Review B **103**, 245102 (2021).
[25] N. M. Gill, C. J. Fontes, and C. E. Starrett, Physical Review E **103**, 043206 (2021).
[26] N. Durante, A. Fortunelli, M. Broyer, and M. Stener, The Journal of Physical Chemistry C **115**, 6277 (2011).
[27] R. J. Magyar, L. Shulenburger, and A. D. Baczewski, Contributions to Plasma Physics **56**, 459 (2016).

[28] A. J. White, L. A. Collins, K. Nichols, and S. X. Hu, Journal of Physics. Condensed Matter **34**, 17 (2022).
[29] A. B. Zylstra *et al.*, Physical Review Letters **114**, 215002 (2015).
[30] Y. H. Ding, A. J. White, S. X. Hu, O. Certik, and L. A. Collins, Physical Review Letters **121**, 145001 (2018).
[31] S. Malko *et al.*, Nature Communications **13**, 2893 (2022).
[32] E. Runge and E. K. U. Gross, Phys. Rev. Lett. **52**, 997 (1984).
[33] N. D. Mermin, Physical Review **137**, A1441 (1965).
[34] W. Kohn and L. J. Sham, Phys. Rev. **140**, A1133 (1965).
[35] T. Sjostrom and J. Daligault, Physical Review B **88**, 195103 (2013).
[36] R. P. Feynman, N. Metropolis, and E. Teller, Physical Review **75**, 1561 (1949).
[37] A. J. White and L. A. Collins, Physical Review Letters **125**, 055002 (2020).
[38] B. Shpiro, M. D. Fabian, E. Rabani, and R. Baer, J. Chem. Theory Comput. **18**, 1458 (2022).
[39] Y. Cytter, E. Rabani, D. Neuhauser, and R. Baer, Phys. Rev. B **97**, 115207 (2018).
[40] M. F. Hutchinson, Communications in Statistics - Simulation and Computation **18**, 3 (2007).
[41] M. D. Feit, J. J. A. Fleck, and A. Steiger, Journal of Computational Physics **47**, 412 (1982).
[42] J. P. Perdew, K. Burke, and M. Ernzerhof, Physical Review Letters **77**, 3865 (1996).
[43] S. Lehtola, C. Steigemann, M. J. T. Oliveira, and M. A. L. Marques, SoftwareX **7**, 1 (2018).
[44] S. Goedecker, M. Teter, and J. Hutter, Phys. Rev. B **54**, 1703 (1996).
[45] C. Hartwigsen, S. Goedecker, and J. Hutter, Phys. Rev. B **58**, 3641 (1998).
[46] M. Krack, Theor Chem Acc **114**, 145 (2005).
[47] S. Zhang *et al.*, Physical Review E **106**, 045207 (2022).
[48] R. Car and M. Parrinello, Physical Review Letters **55**, 2471 (1985).
[49] J. S. Tse, Annual Review of Physical Chemistry **53**, 249 (2002).
[50] L. A. Collins, S. R. Bickham, J. D. Kress, S. Mazevet, T. J. Lenosky, N. J. Troullier, and W. Windl, Physical Review B **63**, 184110 (2001).
[51] A. Mazarro, P. M. Echenique, and R. H. Ritchie, Physical Review B **27**, 4117 (1983).
[52] P. Sigmund and A. Schinner, Journal of Applied Physics **128** (2020).
[53] S. P. Ahlen, Reviews of Modern Physics **52**, 121 (1980).
[54] L. H. Andersen, P. Hvelplund, H. Knudsen, S. P. Möller, J. O. P. Pedersen, E. Uggerhöj, K. Elsener, and E. Morenzoni, Physical Review Letters **62**, 1731 (1989).
[55] S. Smit, in *MultiNonlinearModelFit* (Wolfram Research, https://resources.wolframcloud.com/FunctionRepository/resources/MultiNonlinearModelFit, 2022).
[56] S. X. Hu, L. A. Collins, V. N. Goncharov, J. D. Kress, R. L. McCrory, and S. Skupsky, Phys. Plasmas **23**, 042704 (2016).
[57] S. X. Hu, D. T. Michel, A. K. Davis, R. Betti, P. B. Radha, E. M. Campbell, D. H. Froula, and C. Stoeckl, Physics of Plasmas **23**, 102701 (2016).
[58] S. X. Hu, B. Militzer, V. N. Goncharov, and S. Skupsky, Physical Review Letters **104**, 235003 (2010).
[59] S. X. Hu, L. A. Collins, J. P. Colgan, V. N. Goncharov, and D. P. Kilcrease, Physical Review B **96**, 144203 (2017).
[60] S. X. Hu, B. Militzer, V. N. Goncharov, and S. Skupsky, Physical Review B **84**, 224109 (2011).
[61] S. X. Hu, L. A. Collins, V. N. Goncharov, J. D. Kress, R. L. McCrory, and S. Skupsky, Physical Review E **92**, 043104 (2015).

Figures

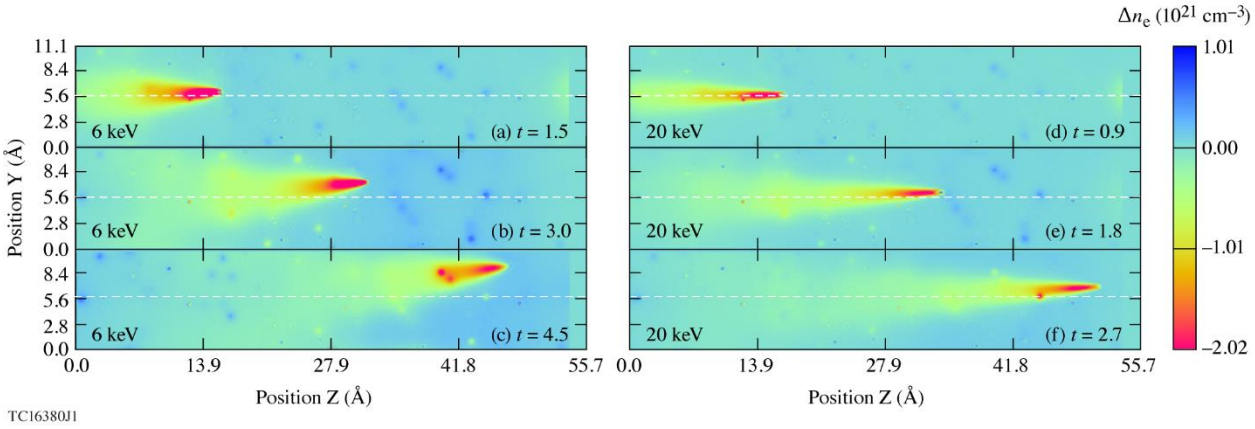

FIG. 1. Two-dimensional snapshot in the y–z plane of the difference between the instantaneous and initial electron density Δn_e [1/cm^3] for a single electron stopping in CH at 0.50 g/cm^3, 500 eV. The panels show the trajectory of the electron as it progresses through the CH and is scattered. Figs. 1(a)–1(c) show time snapshots for an electron projectile with 6 keV initial kinetic energy; Figs. 1(d)–1(f) are time snapshots for an electron with an initial kinetic energy of 20 keV. The lengths of the simulation box are given in angstroms.

.

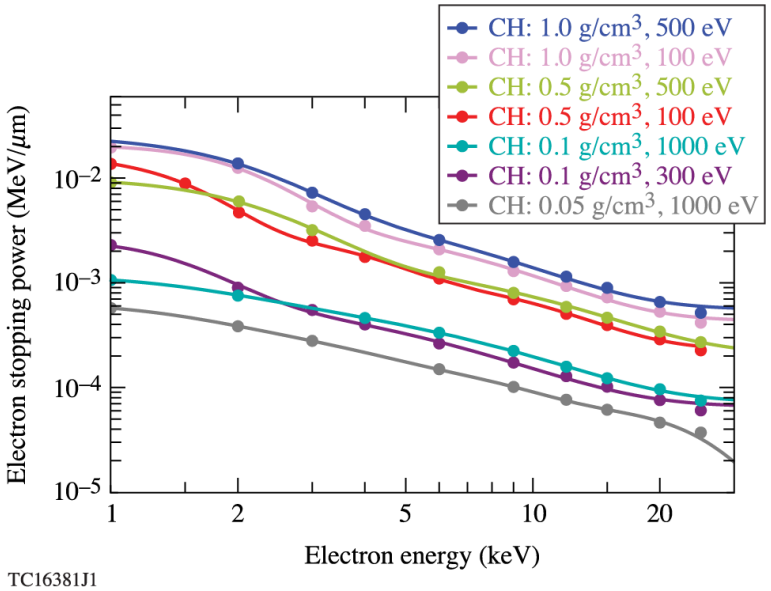

FIG. 2. Electron SP $-dE/dz$, for a high-energy electron stopped in CH plasma as a function of initial electron kinetic energy. The individual points are the TD-OF-DFT calculations; the corresponding curves are the individual fits. The plasma conditions assessed are between 0.05 to 1.0 g/cm^3 and 100 to 1000 eV—conditions relevant to ICF conduction-zone plasmas.

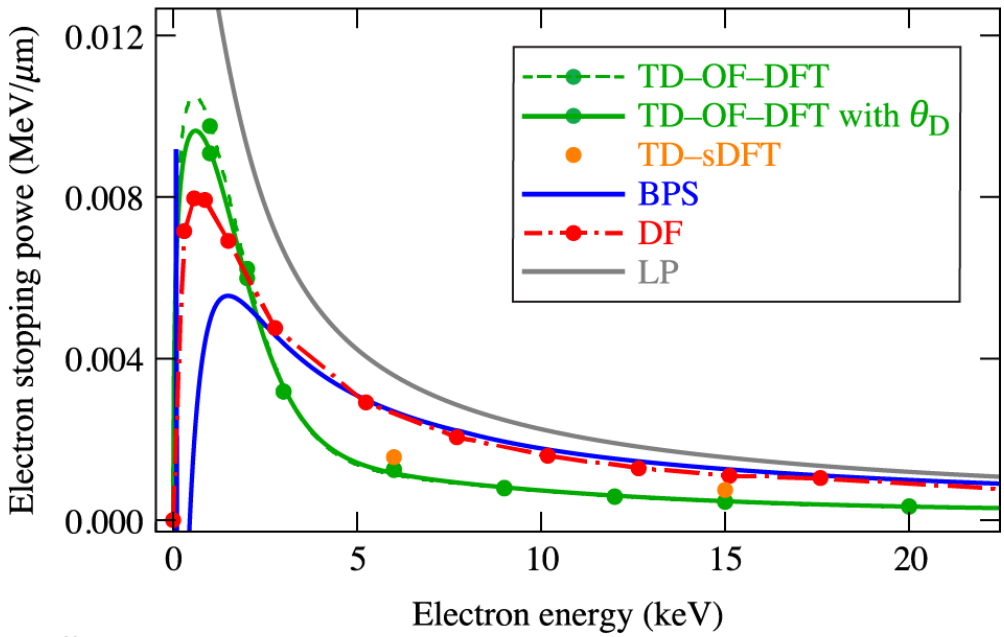

TC16382J1

FIG. 3. ESP in 0.50-g/cm^3, 500-eV CH plasma, with a comparison between the Brown–Preston–Singleton (BPS) (blue), dielectric function (DF) (red), and Li–Petrasso (LP) (gray) analytical models for SP and our TD-DFT data. The solid green curve represents the TD-DFT data with the deflection angle θ_D considered, while the dashed green curve is the TD-DFT data without deflection/scattering considered.

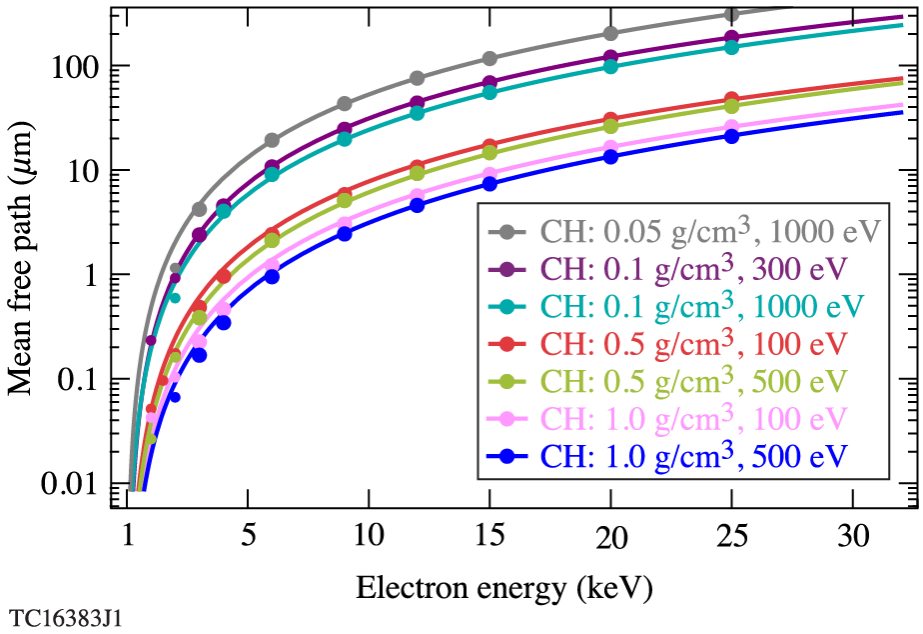

FIG. 4. The nonlocal electron MFP as a function of incoming electron energy. The individual points represent the TD-OF-DFT data shown in Fig. 2., while the solid curves are the corresponding fit for the given plasma conditions and energy. Here the fitting is a global analytical/numerical model as shown in Eq. (12).

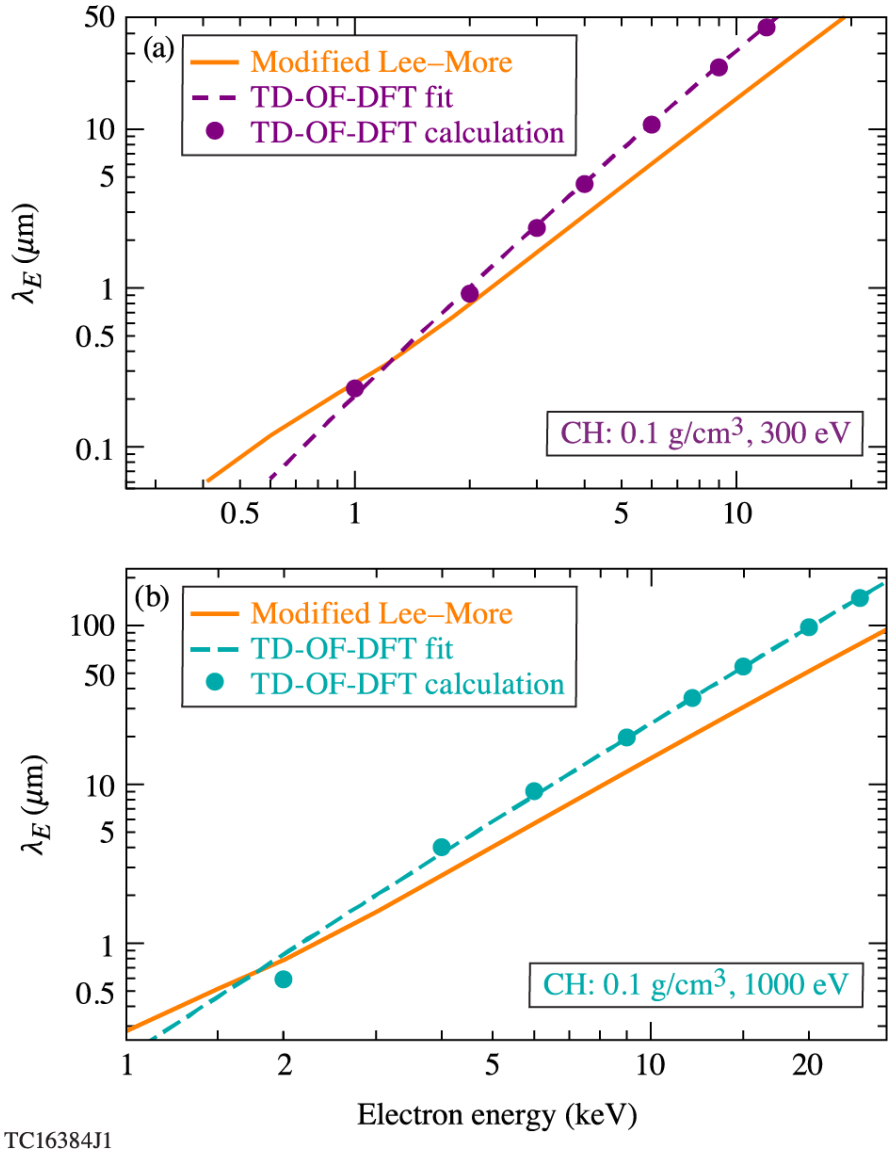

FIG. 5. CH at either (a) 300-eV or (b)-1000 eV plasma temperature and mass density, 0.1 g/cm^3. Comparison between the penetration depth λ_E given by the modified Lee–More method (orange) to the TD-OF-DFT data (individual points) and corresponding fit (blue and purple curves) obtained by fitting the TD-OF-DFT data and given Eq. (12).

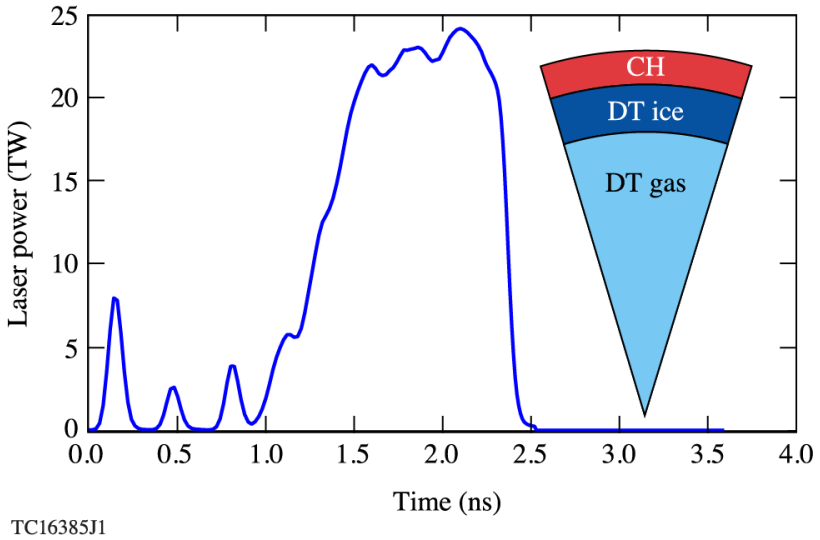

FIG. 6. Laser power as a function of time. Inset: Breakdown of the cryogenic target used in the 1-D hydrodynamic simulation. DT gas (380 μm), surrounded by DT ice (50 μm) and escalated by CH (8 μm). The initial mass density of the CH is 1.05 g/cm^3. For this work, we focus on nonlocal stopping in the CH layer.

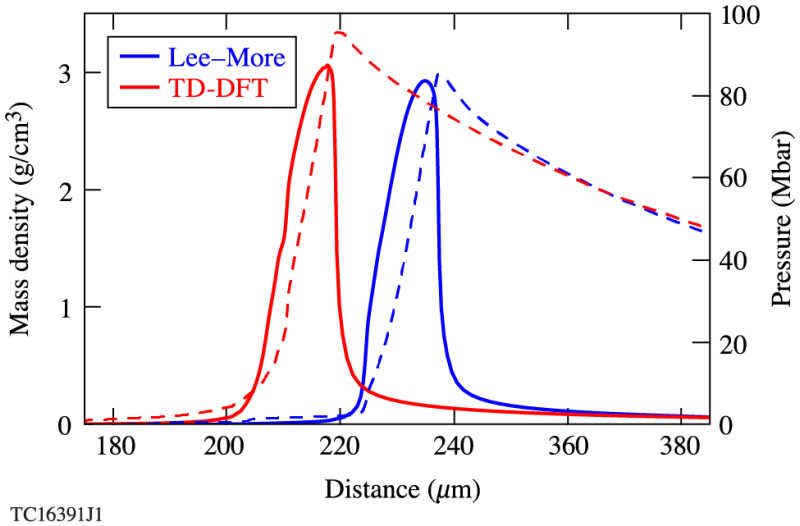

FIG. 7. Comparison at t = 2.1 ns between the mass density (left axis, solid lines) and ablation pressure (right axis, dashed lines) using the TD-DFT model (red) and the modified Lee–More model (blue) for the nonlocal electron transport.

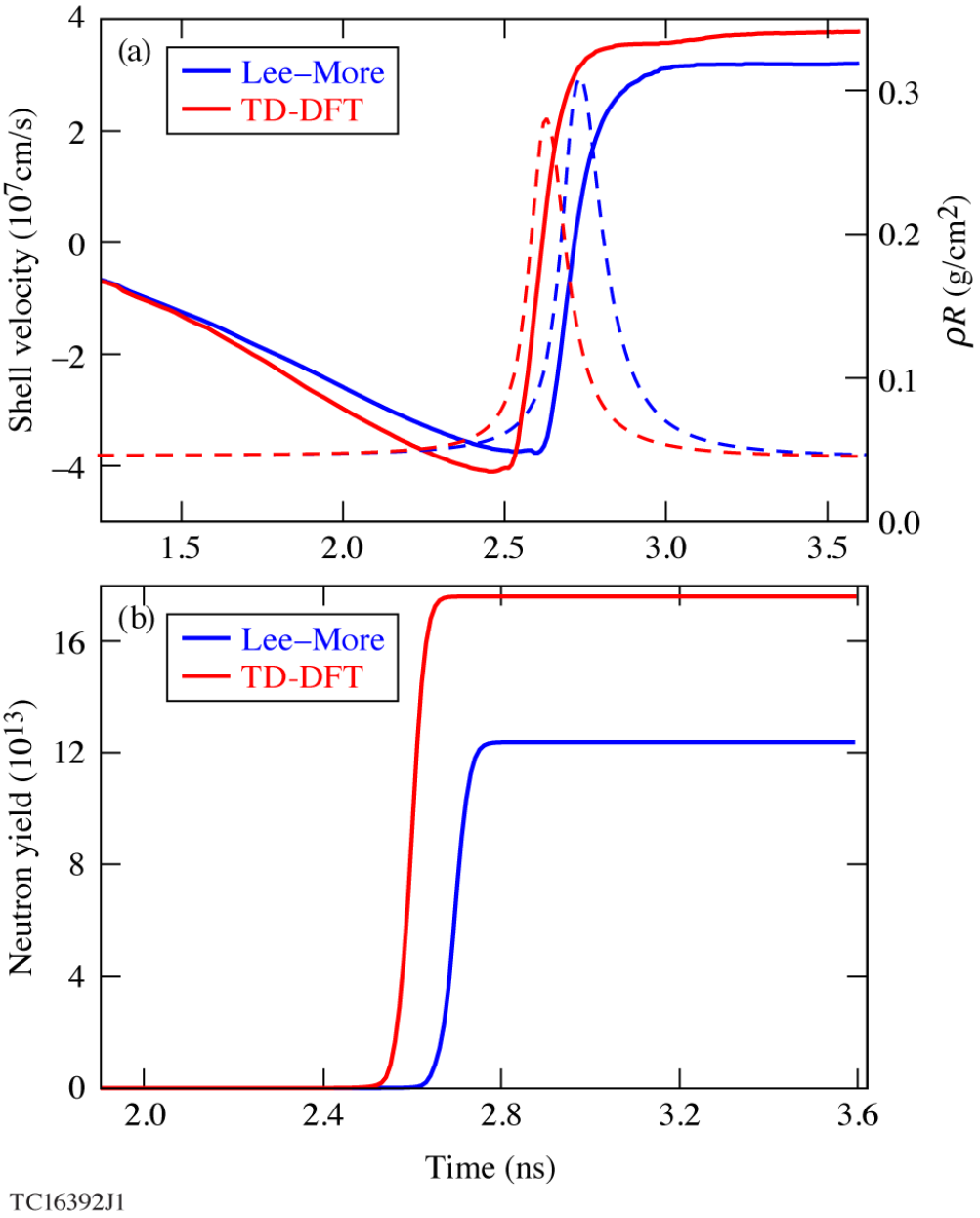

FIG. 8. Comparison of *LILAC* simulation results using the TD-DFT model (red) and the modified Lee–More model (blue) for nonlocal electron transport. Time evolution of (a) the shell velocity (left axis, solid lines) and compression, ρR (right axis, dashed lines) and (b) the neutron yield.

Table

Table I: Numerically determined coefficients (rounded to four significant figures) for the mean-free-path fitting formula given in Eqs. (12) and (13).

$a_0 = 2.685 \times 10^{-15}$	$f_0 = 0.07317$	$\delta = -0.4074$	$\phi_1 = -0.6181$
$b_0 = -0.07709$	$\alpha = 0.3005$	$\varepsilon = 1.431$	$\psi_1 = 1.068$
$c_0 = 6.722 \times 10^{-3}$	$\beta = -0.8279$	$\zeta = -0.7680$	$\phi_2 = -1.068$
$e_0 = 0.02740$	$\gamma = -0.3695$	$\omega = 0.4547$	$\psi_2 = -1.162$